An Active Steering Assistant System for Powered Two-Wheelers

S. Lovato, M. Bova, M. Massaro, M. Andriollo, R. Lot

Abstract—**An active steering assistant (ActiSA) system for powered two wheelers is introduced in this work, with the aim of enhancing the stability and safety of PTW. The proposed technology is alternative to steer-by-wire systems, which have a number of safety issues related to the removal of the mechanical connection between the handlebar and the front frame, and gyroscopic stabilizer, which tend to be heavy, expensive and energy-intensive. The paper illustrates the design and realisation of a steering assistant prototype and the integration in a light electric powered two wheeler. The prototype features an electric motor that provides the (assistant) steering torque to the front frame, which adds to the torque applied by the rider; a custom-steering torque sensor, aimed at monitoring the rider's effort on the handlebar; and a number of off-the-shelf sensors, which monitor the vehicle motion – steering angle, suspensions travel, angular velocity and accelerations of the main frame, rear wheel spin and GPS. Results from functional tests and performance assessment are also discussed.**

Index Terms—**active steering, steering assist, powered two wheelers, motorcycles, eBikes, autonomous vehicle, vehicle dynamics**

I. Introduction

THERE are more than 500 million of powered two-wheelers (PTW, i.e. motorcycles, scooters and mopeds) circulating worldwide and the increasing demand for personal mobility in cities is boosting sales of new vehicles [1]. Compared to cars, PTW offers significant advantages in terms of smaller purchase and running costs, lesser energy demand and noxious emissions, reduced traffic congestions and parking space requirements. However, the safety of PTW users is at stake. Road crashes statistics reveal that vulnerable road users represents more than half of all road casualties, which in 2016 has reached 1.35 million worldwide [2]. In this context, this work aim to reduce the number and severity of PTW road accidents by developing a steering system that stabilises the vehicle in scenarios such as low speed riding, which is a typical urban scenario, and emergency braking.

Vehicle loss of control is related to the intrinsic instability of PTW, which can be associated to three main modes of the motorcycle dynamics: capsize, wobble, and weave [3]–[6]. The capsize mode is characterised by the rollover motion of the vehicle; the wobble mode mainly consists of the oscillation of the steering assembly and may be unstable in the medium speed range; the weave mode consists of oscillation of the whole vehicle and may be unstable both at low and high speed. Stability also depends on the longitudinal acceleration and can be a problem during braking. PTW stabilisers could prevent the loss of control of vehicle and hence reduce the number and severity of accidents. Stabilisation is also a prerequisite for other safety systems such as autonomous emergency braking, which may mitigate two third of crashes [7], [8]. Despite this potential impact, the literature and technique of PTW stabilisers is still in its infancy. So far, two different technologies have been considered: steer-by-wire and gyroscopic stabilisation.

In a steer-by-wire (SbW) system, the direct mechanical connection between the handlebars and the front wheel is replaced by an electro-mechanical system that actively controls the steering. In [9] a SbW control algorithm is described, that is potentially able to stabilise the roll motion, but without experimental validation. In 2017 Honda presented a riding assist prototype which is capable of balancing itself at low and null speed. However, this system includes a complex, variable geometry steering system, whose effectiveness under braking has not been demonstrated. In [10] a steer-by-wire system has been implemented in a bicycle. In a controlled environment, the system successfully supported the rider in performing a slalom, both within the stable and unstable bicycle speed regions. In summary, SbW systems appear to have great potential in stabilizing PTW, on the other hand, the lack of direct mechanical connection between handlebar and the front wheel rises serious safety concerns in case of system failure.

As an alternative to SbW, a gyroscopic stabiliser (GS) is composed of one (or more) flywheel(s) whose precession motion is actively or passively controlled. Research has included the construction of small gyroscopic prototypes [11], the design of feedback controllers to stabilise low-speed capsize motion [12], and analysis of the dynamics of a gyroscopically stabilised vehicle [13]. In 2010, Lit-Motors developed an electric single-track vehicle that is stabilised by a two counter-rotating gyroscopes. However, the system was heavy, power-hungry, and expensive; it newer reached the market. In [14] a systematic analysis on PTW gyroscopic stabilisers is carried out, concluding that actively controlled gyroscopes can stabilise a PTW in its whole range of operating speed, as well as during braking. Moreover, stabilisers are fail safe and it is suggested that they have greater authority that SbW at null and very low speed. However, GS are heavier, more expensive, and request more energy that SbW.

In this work a third technology intended to stabilise PTW is presented, which draws inspiration from the two mentioned above and tries to keep their advantages—stabilization

Manuscript received March 31, 2022; revised April 12, 2022.

S. Lovato: PhD student at the Department of Industrial Engineering, University of Padua, Italy, PD, 35121 — e-mail: stefano.lovato.1@phd.unipd.it.
M. Bova: Research fellow at the Department of Industrial Engineering, University of Padua, Italy, PD, 35121 — e-mail: matteo.bova@unipd.it.
M. Massaro: Associate Professor at the Department of Industrial Engineering, University of Padua, Italy, PD, 35121 — e-mail: matteo.massaro@unipd.it.
M. Andriollo: Associate Professor at the Department of Industrial Engineering, University of Padua, Italy, PD, 35121 — e-mail: mauro.andriollo@unipd.it.
R. Lot: Associate Professor at the Department of Industrial Engineering, University of Padua, Italy, PD, 35121 — e-mail: roberto.lot@unipd.it.

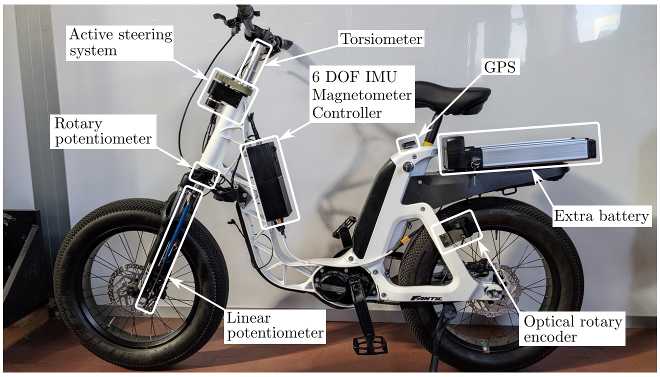

Fig. 1. Layout of the active steering assistant (ActiSA). The steering torque is measured through a specially designed torsiometer, while the other sensors implemented are employed to monitor the vehicle states and feed the controller. The latter provides the control strategy for the steer motor of the active steering system.

capability in wide range conditions—while avoiding the critical issues—system weight, failure safety, and energy consumption. This stabiliser differs from both SbW and GS solutions and consists in an active steering assistant (ActiSA) system that supports the rider to control the vehicle by applying an additional steering torque. The ActiSa is directly connected to the vehicle steering system, without corrupting its structural integrity, i.e. keeping the mechanical connection between the handlebar and the fork.

In Sec. II the ActiSA concept is discussed, together with its fundamental requirements, layout and effects on the vehicle transfer function. The Sec. III focuses on the system hardware implementation. An explanation of the procedures applied to measure the main vehicle characteristics is presented in the first part, followed by a description of the ActiSA components and sensors. Greater emphasis was given to the steering torque sensor (torsiometer), which has been specially designed and calibrated for this application. In addition, the active steering system is characterized under two main aspects: frequency and thermal responses. The former is studied experimentally through a frequency sweep on the input of the motor driver, while the latter is investigated numerically, by feeding a thermal model with experimental data. The functional tests of the system are reported in Sec. IV, which consists of a natural driving session on asphalted ground carried out to prove the prototype reliability. Finally, conclusions are presented in Sec. V, which summarize the main results obtained during the design and construction of the prototype, together with future developments to the ActiSA system.

II. Active steer assistant concept

The aim of this work is to develop and implement an advanced rider assistance system (ARAS) for powered two-wheelers, whose main goal is the vehicle stabilisation in a wide range of operating conditions, especially at low speed. With a target in personal mobility on public roads, the system has to satisfy several requirements, the most important are:

- increasing the vehicle stability;
- preserving the handling characteristics of the vehicle;
- it must be fail-safe, in particular it must not destabilise the vehicle even in case of failure of the controller, sensors, or actuators;
- it should be as light and small as possible;

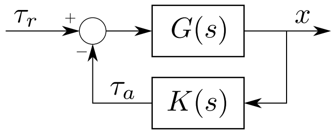

Fig. 2. Block diagram of the ActiSA system. $G(s)$ represents the vehicle transfer function, $K(s)$ is the ActiSA transfer function, τ_r, τ_a are the torque applied by the rider and by the controller, respectively, while x corresponds to the vehicle states.

- power consumption should be as small as possible.

In Sec. I the two main alternative solutions devised so far are described: gyroscopic stabilisers (GS) and steer-by-wire (SbW) systems. In this paper a third alternative is developed, that consists in an active steering assistant (ActiSA) which applies a steering torque between the vehicle chassis and the front assembly, such as in a SbW system. However, the rigid connection between the handlebar and the fork is kept, so that the system controls the vehicle in parallel with the rider, as in a GS system.

The ActiSA system is illustrated in Fig. 1 and includes a set of sensors (perception layer), a data-logger and digital controller (decision layer), and a motor-drive (action layer). The latter is fixed to the vehicle chassis and connected to the steering system through a planetary gearbox and a belt transmission.

Since PTW stability is influenced by the vehicle speed, the controller algorithms available in literature typically have the form of linear feedback laws on various states of the system (usually roll angle/rate, yaw rate, and steer angle/rate).

While stabilising the vehicle, the control system has to cooperate with the human rider, which is in charge of the guidance task instead. The system is represented with a closed loop block diagram shown in Fig. 2, where x is the vector of states, τ_r and τ_a are the human rider and assistance steering torque inputs respectively, $G(s)$ is the vehicle transfer function and $K(s)$ that of the ActiSA controller. The overall transfer function can be written as

$$H(s) = \frac{G(s)}{1 + K(s) \cdot G(s)}. \tag{1}$$

An important requirement is that the ActiSA system must not significantly alter the handling characteristic of the vehicle, which are represented by the transfer function $G(s)$. In other words, while the control system $K(s)$ must ensure the vehicle stability, the closed-loop stability transfer function $H(s)$ described in (1) should remain similar to $G(s)$.

Another fundamental requirement for the ActiSA system concern the possibility for the rider to override the active steering system, e.g. in case of controller failure. To ensure this condition, the maximum steering torque applied by the ActiSA on the vehicle must be limited to values well below the typical capability of human riders.

III. Hardware implementation

The baseline vehicle used to build the ActiSA prototype is the Fantic ISSIMO Urban e-bike. This bicycle weighs approximately 36 kg and is equipped with a 250 W electric motor for pedal assistance. In Fig. 1 the hardware scheme, together with the baseline vehicle, is shown. Three subsystems can be identified: the active steering system, the rider steering

ISBN: 978-988-14049-3-0
ISSN: 2078-0958 (Print); ISSN: 2078-0966 (Online)

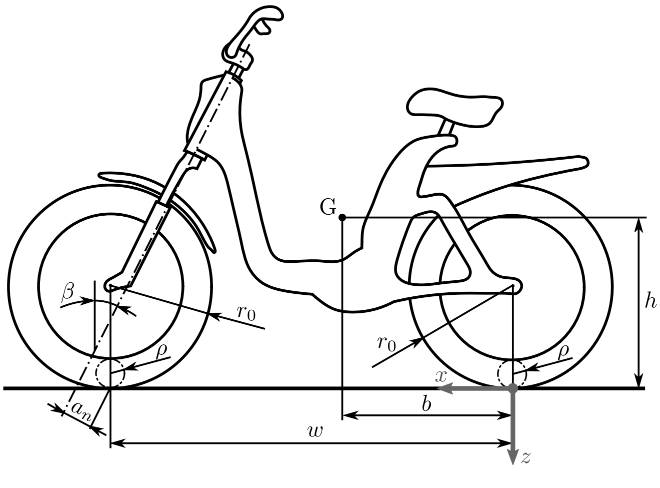

Fig. 3. Side view of the vehicle with the main vehicle characteristics. The vehicle has wheelbase w, while the longitudinal and vertical positions of the centre of mass are b and h. For both tires, the unloaded radius and the cross-section radius are r_0 and ρ, respectively. The steer has caster angle β and normal trail a_n. The vehicle reference system is located at the rear contact point, with the x axis pointing forward and the z axis downwards.

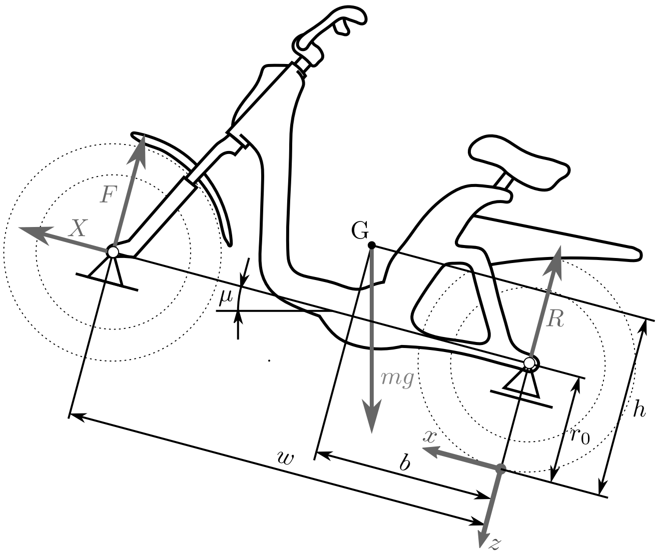

Fig. 4. Centre of mass measurement system. The forces F, R are measured by using load cells with the vehicle pitched at different angles μ.

torque measure system, and the vehicle motion measurement system. All the sensors signals are then collected with Teensy 4.1 micro-controller unit (MCU) running at 1 kHz, which deals with data logging and control loop execution.

A. Vehicle characteristics

Both the sizing of the active steering system and the design of the control logic require a knowledge of the main physical characteristics of the vehicle plus rider system, such as the geometrical and inertial properties. These are in fact fundamental for estimating the response of the system to rider inputs (i.e. $G(s)$ in Fig. 2). The vehicle is modelled with 4 rigid bodies shown in Fig. 3: rear and front wheels, chassis and handlebar. The tyres are characterized by a toroidal shape. The inertial parameters of the system are described by the location of the centre of mass (point G in Fig. 3) together with its inertia tensor, the mass of each wheel and the related inertias—the wheel axial inertia is especially relevant when it comes to gyroscopic effects. The rider model is taken from [15], which gives the estimation of its centre of mass and inertia tensor as functions of rider mass, height and posture on the vehicle. The results of the measurements and estimations performed are reported in Tab. I-II.

The position of the centre of mass was measured using a test-rig available in the university laboratory. This consists of a rigid frame, two load cells fixed to the frame and two adjustable to fit the vehicle wheelbase, an inclinometer, and a hydraulic lifting system. For the estimation of the longitudinal b and vertical h positions of the center of mass (with respect to the rear contact point), the vehicle is pitched at different angles by lifting the rigid frame. For each inclination the equilibrium equation around the pitch axis gives

$$F\,(w-b) - Rb + (h-r_0)\,(F+R)\tan\mu = 0, \qquad (2)$$

where w is the vehicle wheelbase, r_0 the unloaded tire radius, F and R are the front and rear forces measured by the load cells, and μ is the pitch angle; see Fig. 4.

The determination of the centre of mass position requires the measurement of the vertical loads F, R with at least two tests at different inclinations, which allow to write (2) for the two inclinations and to solve for h and b. Alternatively, multiple inclinations can be tested and the corresponding (measured) F_i, R_i fitted applying the least-square method as follows

$$\min \sum_{i=1}^{n} \left(F_i\,(w-b) - R_i b + (h-r_0)\,(F_i+R_i)\tan\mu_i\right)^2, \qquad (3)$$

where n is the number of acquisitions. The minimisation of Eq. 3 can be addressed by enforcing to zero the partial derivatives with respect to h and b, to give

$$\sum_{i=1}^{n}\left(\begin{bmatrix} (F_i+R_i)^2 & -(F_i+R_i)^2\tan\mu_i \\ -(F_i+R_i)^2\tan\mu_i & (F_i+R_i)^2\tan^2\mu_i \end{bmatrix}\right)\cdot \begin{bmatrix} b \\ h \end{bmatrix} = \sum_{i=1}^{n}\begin{bmatrix} F_i\,(F_i+R_i)\,w - (F_i+R_i)^2 r_0\tan\mu_i \\ -F_i\,(F_i+R_i)\,w\tan\mu_i + (F_i+R_i)^2 r_0\tan^2\mu_i \end{bmatrix}, \qquad (4)$$

which can be solved for h and b.

This procedure has been applied in this work with 75 inclinations and residual 0.05 N^2, obtaining the results reported in Tab. I. The lateral position (y coordinate) of the centre of mass is assumed equal to zero as the vehicle model is symmetrical with respect to the x-z plane.

The normal trail a_n was measured by using photos of a side view of the Issimo. Some precautions have been taken in order to reduce the distortion of the photographs, such as keeping an adequate distance from the vehicle and using the camera zoom. The estimation was carried out assuming the wheelbase w shown in Tab. I. This technique was also used to estimate the unloaded radius r_0 (equal for both front and rear tires) and the caster angle β, that is the angle between the steering axis and the normal to the road surface.

The tire rolling radius r_r was estimated by moving the bicycle, measuring the number of rotations of the wheels N_{rev} and the corresponding travelled distance L. The rolling

TABLE I
FANTIC ISSIMO URBAN E-BIKE CHARACTERISTICS WITH STEERING ASSIST SYSTEM.

Parameter	Vehicle	Rider	Overall	Units	Description
m	36.0	65.0	101.0	kg	mass
w	1.149	-	-	m	wheelbase
b	0.483	0.348	0.396	m	longitudinal position of the centre of mass w.r.t. the rear contact point
h	0.459	1.015	0.817	m	height of the centre of mass w.r.t. the rear contact point
I_x	1.3	6.8	15.2	$\mathrm{kg\,m^2}$	roll inertia w.r.t. the respective centre of mass
I_y	6.5	6.8	20.8	$\mathrm{kg\,m^2}$	pitch inertia w.r.t. the respective centre of mass
I_z	5.4	2.7	8.5	$\mathrm{kg\,m^2}$	yaw inertia w.r.t. the respective centre of mass
I_{xz}	0.6	1.3	3.6	$\mathrm{kg\,m^2}$	product of inertia w.r.t. the respective centre of mass
β	26.5			deg	caster angle
a_n	0.082			m	normal trail
r_0	0.300			m	tire unloaded radius
r_r	0.295			m	tire rolling radius
ρ	0.06			m	tire torus radius
m_f	3.6			kg	front wheel mass
I_{af}	0.152			$\mathrm{kg\,m^2}$	front wheel axial inertia
I_{df}	0.083			$\mathrm{kg\,m^2}$	front wheel diametrical inertia
m_r	5.0			kg	rear wheel mass
I_{ar}	0.152			$\mathrm{kg\,m^2}$	rear wheel axial inertia
I_{dr}	0.085			$\mathrm{kg\,m^2}$	rear wheel diametrical inertia

Fig. 5. Tire torus radius measurement system. A variable number of equally spaced screws are slid along a guide until they reach the surface of the tire. The measurement of the screw depth provides the y coordinate of the toroid profile, while its relative position the x coordinate.

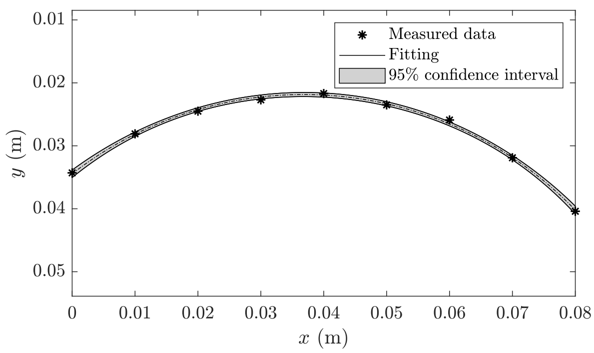

Fig. 6. Results of the torus radius measurement with the fitting circumference.

radius is then given by

$$r_r = \frac{L}{2\pi N_{rev}}. \tag{5}$$

The test was performed at very low speed, obtaining the value in Tab. I.

Fig. 5 shows the measurement system used to estimate the tire torus radius ρ. The data collected consists of the x, y coordinates of 10 points across the tire cross section. The x,y values were fitted using a circumference with the center position and its radius as unknown parameters, to give the value in Tab. I; see Fig. 6.

An important characteristic of a bicycle is represented by the moments of inertia of the wheels, especially the axial component which mainly influences the tire gyroscopic effects. The estimation of both axial and diametral moment of inertia has been carried out through a trifilar pendulum approach [16] and the results are reported in Tab. I. The vehicle used in this work presents identical tires and rims, and the slight differences between the two wheels are due to the presence of the shifting gear mounted at the rear axle, which increases the wheel mass and diametrical inertia.

The vehicle roll, pitch and yaw moments of inertia with respect to the centre of mass have been estimated indirectly. The geometry of the main vehicle components have been measured and a simplified model has been designed, consisting of 14 segments characterized by simple cylinders and toroids. The segment parameters were then adjusted to reproduce the measured centre of mass location. Finally, the vehicle inertial characteristics variation due to the presence of a rider have been estimated by adding to the model described above the multibody rider model from [15]; see Tab. I. The anthropometric model selected is the suggested *Zatsiorsky-DeLeva-Model*, assuming the rider parameters in Tab. II.

B. Steering torque sensor

The measurement of the steering torque applied by the rider required the design of a torsiometer integrated with the steering shaft, as shown in Fig. 7 (left). This sensor consists of a lathed aluminium shaft on which an HBM 3/350-VY43 strain gauge is applied. This has a full-bridge configuration with the strain gauges at 45 deg with respect to the shaft axis, in order to reject temperature influence together with the axial and shear stress components, while focusing on the twisting component. The strain gauges are then connected to a 2038-1 MecoStrain amplifier module. The additional handlebar height caused by the installation of the torsiometer

ISBN: 978-988-14049-3-0
ISSN: 2078-0958 (Print); ISSN: 2078-0966 (Online)

TABLE II
RIDER PARAMETERS FOR THE ANTHROPOMETRIC MODEL.

Description	Value	Units
Rider mass	65	kg
Rider height	1.75	m
Handlebar x, y, z coordinates (w.r.t. the rear contact point)	0.70, 0.36, -1.10	m
Pedal x, y, z coordinates (w.r.t. the rear contact point)	0.20, 0.17, -0.30	m
Saddle x, y, z coordinates (w.r.t. the rear contact point)	0.56, 0.00, -0.85	m
Elbow-to-elbow distance	0.60	m
Knee-to-knee distance	0.30	m
Rider lean angle	10	deg

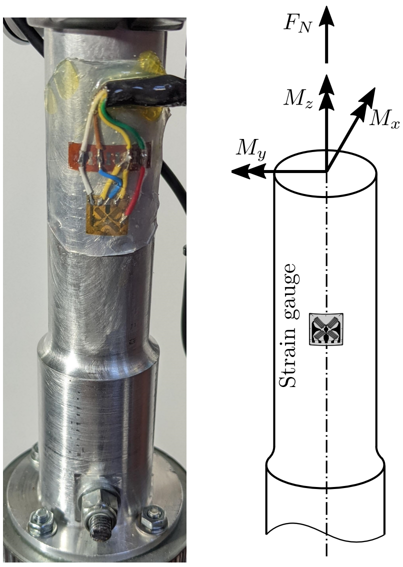

Fig. 7. Torsiometer integrated with the handlebar (left), consisting of a lathed aluminium shaft and a Wheatstone-bridge configuration strain gauge. Schematic representation (right) of the forces and torques applied to the torsiometer during the testing phase.

was recovered by changing the handlebar itself, thus ensuring a driving position very close to the original one.

The torsiometer required a calibration prior to its implementation. Assuming that the sensor exhibits a linear response, calibration involves the identification of each element of its sensitivity matrix. The equation that relates the measured output voltage and the forces and torques applied to the torsiometer (see Fig. 7, right) can be written as

$$V = a \cdot F_N + b \cdot M_x + c \cdot M_y + d \cdot M_z + e, \tag{6}$$

where V is the measured output voltage of the amplifier module, F_N is the axial load, $M_{x,y}$ are the two bending moments and M_z is the twisting torque.

The torsiometer was tested for each load component described above, proving that the coefficients a, b, c are much smaller than d and therefore may be neglected. Eq. (6) can now be rewritten isolating the twisting torque as

$$M_z = \frac{1}{d} \cdot (V - e) = m \cdot (V - e) \,. \tag{7}$$

To determine the value of the slope m and the offset e, a variable torque has been applied to the torsiometer by changing the axial distance of a fixed weight, measuring the strain gauge output voltage at each step. The maximum torque applied is approximately 25 Nm, which is greater than

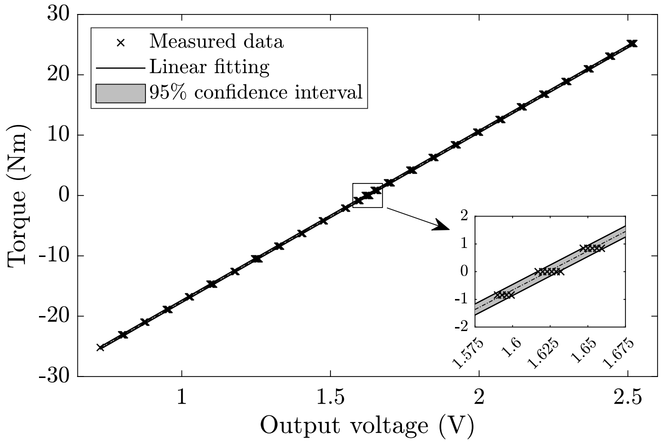

Fig. 8. Results of the torsiometer calibration. A variable torque has been applied to the torsiometer, measuring the strain gauge output voltage at each step.

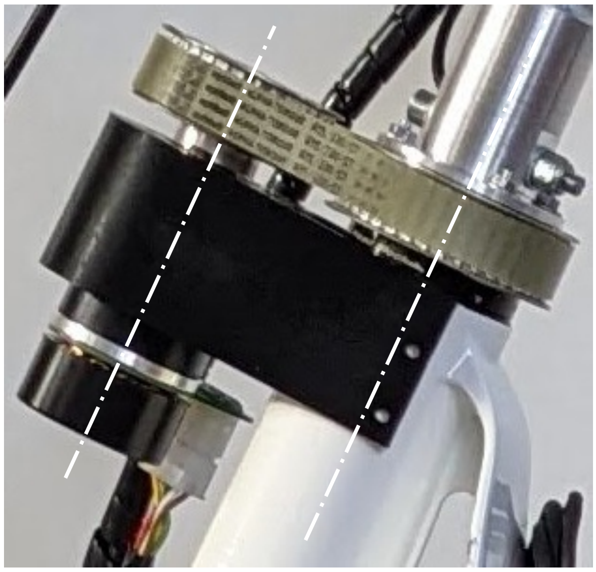

Fig. 9. Active steering system installed on the vehicle. A Maxon EC45 brushless DC motor coupled with a Maxon GP42C planetary gearhead (36:1 reduction ratio) is connected to the handlebar through a belt transmission (1.25:1 reduction ratio).

the typical steering torque produced by a rider. The results of the described procedure are reported in Fig. 8. These results demonstrate negligible hysteresis and a linear response of the sensor. By fitting the measured data, the torsiometer calibration parameters (slope and offset) can be identified and (7) can be finally rewritten as

$$M_z = 28.2 \cdot (V - 1.624) \pm 0.2 \qquad (95\%), \tag{8}$$

where the measured voltage is expressed in V and the twisting torque is expressed in Nm.

C. Active steering system

The active steering system consists of a Maxon EC45 brushless DC motor coupled with a Maxon GP42C planetary gearhead, with a 36:1 reduction ratio. An additional belt drive transmission with 1.25:1 reduction ratio is added to transfer the torque form the motor shaft to the vehicle handlebar. The motor stator is then fixed to the chassis through a specially designed support, as shown in Fig. 9.

ISBN: 978-988-14049-3-0
ISSN: 2078-0958 (Print); ISSN: 2078-0966 (Online)

TABLE III
ACTIVE STEERING SYSTEM CHARACTERISTICS.

Parameter	Value	Units	Description
P	70	W	brushless motor power
V_{cc}	24	V	supply voltage
τ_1	36		planetary gearbox reduction ratio
τ_2	1.25		belt transmission reduction ratio
T_{cc}	6	Nm	continuous output torque
T_{max}	14	Nm	peak output torque

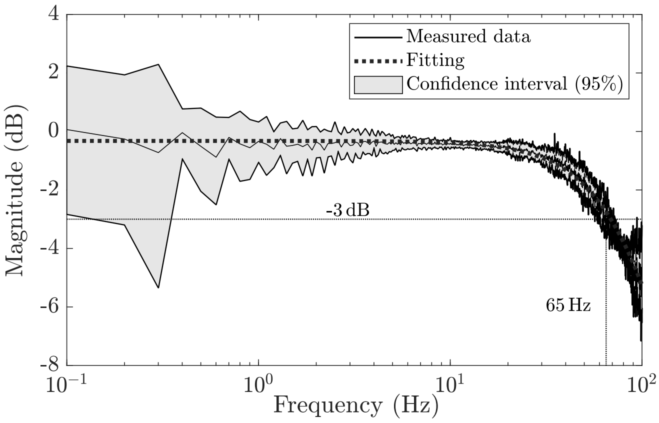

Fig. 10. Frequency response function of the active steering system. The FRF is fitted with a second-order low-pass filter.

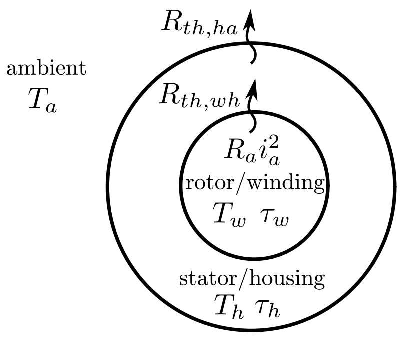

Fig. 11. Thermal model of the motor used in the thermal response investigation.

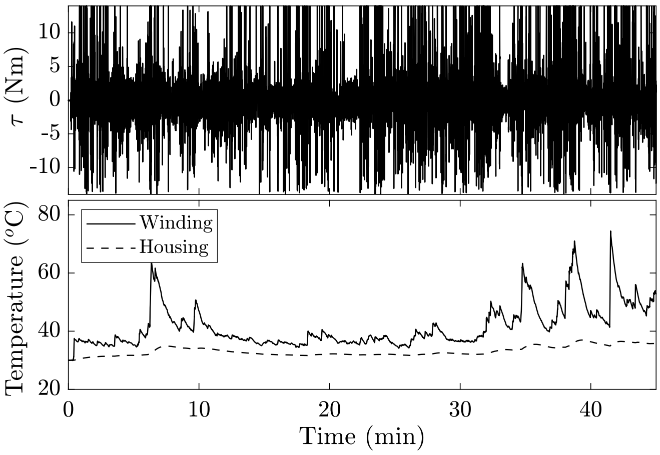

Fig. 12. Thermal response of the active steering system: motor torque input (top), and winding and housing outputs (bottom).

This configuration allows a continuous torque around 6 Nm and a maximum instantaneous torque of 14 Nm, which is below the maximum capability of human riders, for safety reasons. In addition to the applied steering torque, through the motor controller the steer rate can be measured. In order to avoid to affect the battery management system already installed on the vehicle, an extra battery (shown in Fig. 1) has been added to power the active steering system and all the sensors.

The active steering system (gearbox-motor-driver) has been characterized, taking into consideration two main aspects: frequency response and thermal response.

1) Frequency response function: The active steering system (gearbox-motor-driver) frequency response function (FRF) between the actual motor current—proportional to the assistance steering torque—and the reference motor current—the input of the motor driver—has been investigated experimentally by imposing a sinusoidal input signal, with the frequency sweep from 0 Hz up to 125 Hz. The frequency response obtained is reported in Fig. 10, along with a 95 % confidence interval generated by repeating the procedure 30 times. The trend of the experimental frequency-response-function follows that of a second-order low-pass filter with a bandwidth up to 65 ± 5 Hz (which is enough for the application described in this work), and can be fitted by

$$T(s) = \frac{K}{(1+\tau s)^2}, \tag{9}$$

where K is the filter gain, while τ corresponds to the time constant. The resulting fitting parameters are $K = 0.965 \pm 0.005$ and $\tau = (1.43 \pm 0.06) \cdot 10^{-3}$ s, at a 95% confidence interval.

2) Thermal characterisation: The thermal response of the motor has been investigated numerically by employing the thermal model shown in Fig. 11. This consists of two bodies representing the rotor/winding and the stator/housing, with temperatures T_w, T_h and thermal time constants τ_w, τ_h, respectively. The heating is generated by the Joule effect due to the winding resistance. The heat exchange occurs from the winding to the housing—through the thermal resistance $R_{th,wh}$—and from the housing to the ambient—through the thermal resistance $R_{th,ha}$. The model equations can be written as follows

$$\begin{aligned} \tau_w \dot{T}_w + (T_w - T_h) &= R_{th,wh} R_a(T_w) i_a^2, \\ \tau_h \dot{T}_h + (T_h - T_a) &= \frac{R_{th,ha}}{R_{th,wh}} (T_w - T_h), \\ R_a(T_w) &= R_0(1 + \alpha(T_w - T_0)), \end{aligned} \tag{10}$$

where T_a is the ambient temperature, R_a, R_0 are the motor terminal resistance at T_w and $T_0 = 20\,^o$C, α the temperature coefficient of resistance (assumed equal to $0.004\,^o\mathrm{C}^{-1}$ for copper) and i_a the motor current. The latter can be estimated as

$$i_a = \frac{\tau}{\tau_1 \tau_2 \eta k_t}, \tag{11}$$

where τ is the handlebar torque given as input from logged data, η is the transmission efficiency (assumed equal to 0.8), k_t is the motor torque constant. All the previous described parameters values have been taken from the motor datasheet. The winding and housing temperature are reported in Fig. 12 as a function of time, along with the torque used to feed

ISBN: 978-988-14049-3-0
ISSN: 2078-0958 (Print); ISSN: 2078-0966 (Online)

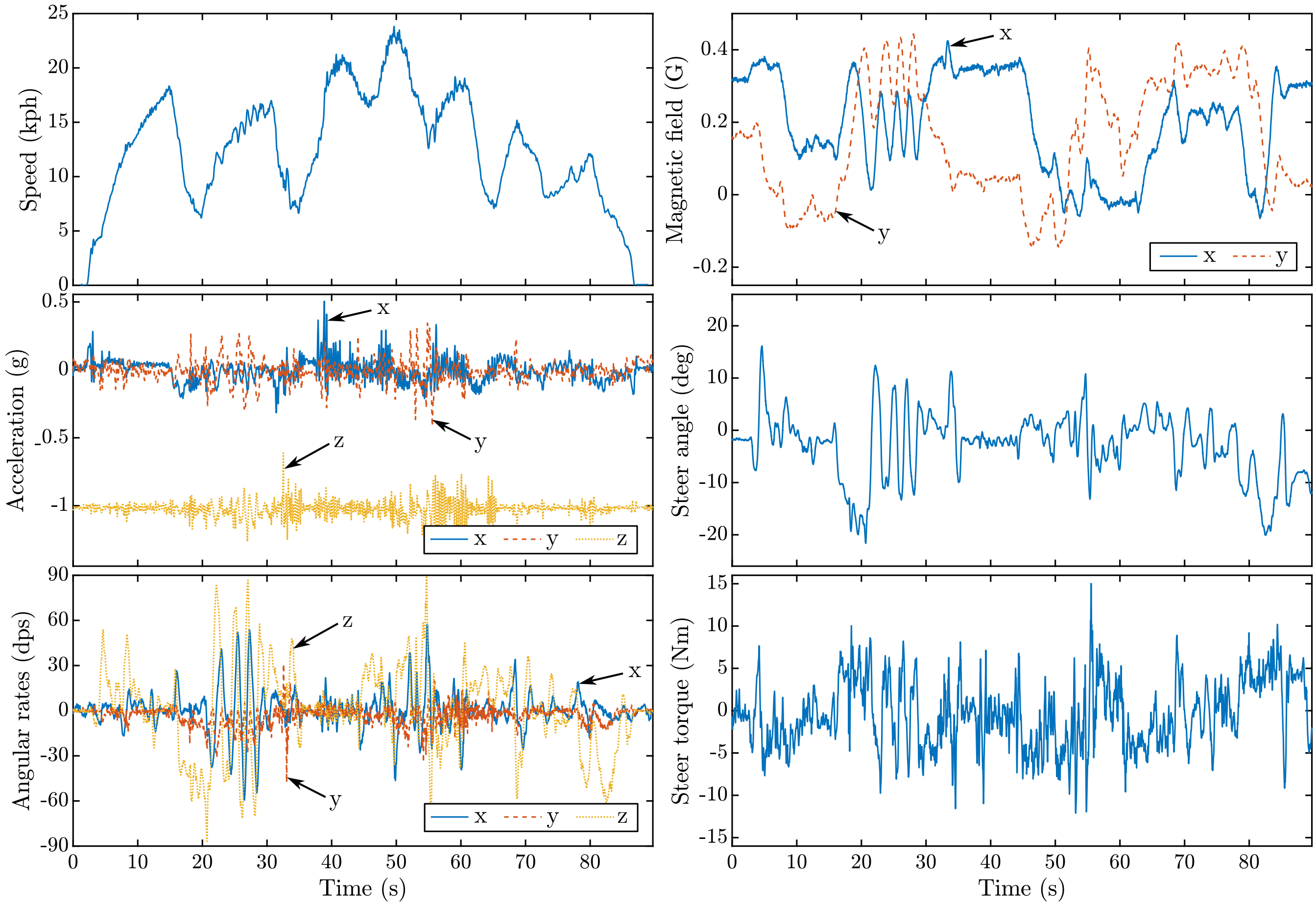

Fig. 13. Logged signals from the functional test.

TABLE IV
CHARACTERISTICS OF VEHICLE MOTION SENSORS

Parameter	Sensor	Characteristics
steer angle	rotary potentiometer	resistance: 3 kΩ range: 100 deg
fork travel	SLS130/150	resistance: 6 kΩ stroke: 150 mm
speed	rotary optical encoder	counts per revolution: 100 3 output signals (A, B, Z)
GPS	Adafruit Ultimate GPS	position accuracy: 1.8 m update rate: 10 Hz
magnetic field	LIS3MDL	magnetic range: $\pm 4\,G$ update rate: $200\,Hz$
acceleration and angular velocity	ISM330DHCX	a range: $\pm 19.6\,\mathrm{m/s^2}$ ω range: ± 2000 deg/s update rate: $3333\,Hz$

the thermal model. This is limited to 14 Nm, which is the peak torque of the active steering system, and has a frequency content up to $2 \div 3$ Hz, consistent with the motor-driver bandwidth. With an ambient temperature of 30 ^{o}C, the simulation shows a housing temperature around 35 ^{o}C and a peak winding temperature around 75 ^{o}C, below the maximum allowed by the datasheed.

D. Vehicle motion sensors

Additional sensors are implemented to monitor the gross motion of the vehicle, see Fig. 1. More in details, the steer angle is measured through a rotary potentiometer installed on the steering head, which allows a range of approximately ±30 deg. The front suspension travel is measured with a SLS130 linear displacement sensor with a maximum stroke of 150 mm. The vehicle speed is measured using an optical rotary encoder with 100 counts/revolution mounted on the rear wheel rim. The encoder output consists of three signals: two signals A/B with fixed phase shift used to determine the rotation direction and speed, and a signal Z used to compute the travelled distance.

A GPS module gives the position of the bicycle in longitude/latitude coordinates while a LIS3MDL 3-axis magnetometer is used to determine the magnetic field. Finally, a ISM330DHCX 6-axis inertial measurement unit (IMU) is installed inside the MCU box to measure the chassis translational accelerations and angular velocity components. These signals, together with the measured speed, steering position and rate, may be potentially used in the real time estimation of the vehicle roll and yaw angle.

IV. Functional Test

Once assembled the prototype, some experimental tests were carried out to prove the system reliability and data acquisition. The test consisted of a natural driving session on asphalted ground lasting roughly a minute and a half. Fig. 13 shows the main signals logged during the functional test, expressed as a function of time. After 15 s of straight motion to increase speed, a short slalom manoeuvre (about 10 s) was carried out. This is clearly distinguishable in Fig. 13, especially in the magnetic field plot, between 20 and 30 s.

ISBN: 978-988-14049-3-0
ISSN: 2078-0958 (Print); ISSN: 2078-0966 (Online)

After that, some hard accelerations and braking manoeuvres have been made to check sensor holders reliability, avoiding wheelie and stoppie (i.e. lifting the rear or the front wheel from the ground). The peak speed is approximately 25 kph (limited by the e-bike motor driver), while the peak accelerations are approximately 0.63, 0.55 and 0.39 g (net of gravity) for the longitudinal, lateral and vertical direction respectively. The corresponding accelerations RMSs are 0.095, 0.092 and 0.110 g on the same axes. The x (roll) and z (yaw) axes angular velocity components reach their peak during the slalom manoeuvre, equal to 59.4 dps and 89.7 dps respectively. The y (pitch) axis component reaches the peak value of 47.7 dps during the repeated accelerations test instead. The RMS steer torque applied by the rider is 4 Nm, with values mostly below 12 Nm and a peak value of 15 Nm. These values are consistent with those of the active steering system (see Tab. III).

V. Conclusion

In this work an active steering assistant system (ActiSA) primarily intended to stabilize powered two wheelers has been presented both in its conceptualization and its prototyping. The vehicle plus rider system model has been designed, starting from measurements and estimations on a real vehicle. The ActiSA system has been then characterized both in terms of frequency response (experimentally) and thermal response (numerically). The steering torque applied by the rider (which is the model input) is measured through a specifically designed and calibrated torsiometer integrated with the vehicle handlebar. Finally, a brief functional test is described, which aims to test the prototype reliability and show the capability of the on-board instrumentation.

References

[1] W. H. Organization, *Powered two- and three-wheeler safety: a road safety manual for decision-makers and practitioners*. World Health Organization, 2017.

[2] ——, *Global status report on road safety 2018: Summary*. World Health Organization, 2018.

[3] R. Lot and J. Sadauckas, *Motorcycle Design: vehicle dynamics concepts and applications*. Lulu.com, 2022.

[4] D. J. N. Limebeer and M. Massaro, *Dynamics and optimal control of road vehicles*. Oxford, UK: Oxford University Press, 2018.

[5] A. L. Schwab, J. P. Meijaard, and J. D. G. Kooijman, "Lateral dynamics of a bicycle with a passive rider model: Stability and controllability," *Vehicle System Dynamics*, vol. 50, no. 8, pp. 1209–1224, 2012.

[6] R. Sharp, S. Evangelou, and D. J. Limebeer, "Advances in the modelling of motorcycle dynamics," *Multibody system dynamics*, vol. 12, no. 3, pp. 251–283, 2004.

[7] G. Savino, F. Giovannini, N. Baldanzini, M. Pierini, and M. Rizzi, "Assessing the potential benefits of the motorcycle autonomous emergency braking using detailed crash reconstructions," *Traffic Injury Prevention*, vol. 14, no. sup1, pp. S40–S49, 2013, pMID: 23905921. [Online]. Available: https://doi.org/10.1080/15389588.2013.803280

[8] G. Savino, R. Lot, M. Massaro, M. Rizzi, I. Symeonidis, S. Will, and J. Brown, "Active safety systems for powered two-wheelers: A systematic review," *Traffic Injury Prevention*, vol. 21, no. 1, pp. 78–86, 2020.

[9] Y. Marumo and M. Nagai, "Steering control of motorcycles using steer-by-wire system," *Vehicle System Dynamics*, vol. 45, no. 5, pp. 445–458, 2007.

[10] G. Dialynas, A. Schwab, and R. Happee, "Design and implementation of a steer-by-wire bicycle," in *International Cycling Safety Conference*, 11 2018.

[11] A. V. Beznos, A. M. Formal'sky, E. V. Gurfinkel, D. N. Jicharev, A. V. Lensky, K. V. Savitsky, and L. S. Tchesalin, "Control of autonomous motion of two-wheel bicycle with gyroscopic stabilisation," in *Proceedings. 1998 IEEE International Conference on Robotics and Automation (Cat. No.98CH36146)*, vol. 3, 1998, pp. 2670–2675.

[12] D. Karnopp, "Tilt control for gyro-stabilized two-wheeled vehicles," *Vehicle System Dynamics*, vol. 37, no. 2, pp. 145–156, 2002.

[13] S. C. Spry and A. R. Girard, "Gyroscopic stabilisation of unstable vehicles: configurations, dynamics, and control," *Vehicle System Dynamics*, vol. 46, no. sup1, pp. 247–260, 2008.

[14] R. Lot and J. Fleming, "Gyroscopic stabilisers for powered two-wheeled vehicles," *Vehicle System Dynamics*, vol. 57, no. 9, pp. 1381–1406, 2019.

[15] M. Bova, M. Massaro, and N. Petrone, "A three-dimensional parametric biomechanical rider model for multibody applications," *Applied Sciences*, vol. 10, no. 13, 2020. [Online]. Available: https://www.mdpi.com/2076-3417/10/13/4509

[16] G. Hughes, "Trifilar pendulum and its application to experimental determination of moments of inertia," *ASME Papers*, vol. 57, 1957.

ISBN: 978-988-14049-3-0
ISSN: 2078-0958 (Print); ISSN: 2078-0966 (Online)